Research Square

Preprints are preliminary reports that have not undergone peer review.
They should not be considered conclusive, used to inform clinical practice,
or referenced by the media as validated information.

Mouse genetic mosaic model for basal-like breast cancer reveals disruption of basal-myoepithelial architecture at premalignancy

Alexys T. Riddick
University of Virginia
Xian Zhou
University of Virginia
Kevin A. Janes
University of Virginia
Hui Zong
hz9s@virginia.edu

University of Virginia

Research Article

Keywords: basal-like breast cancer, premalignancy, basal-myoepithelial architecture, whole-mount imaging, mouse genetic mosaic model

Posted Date: October 29th, 2026

DOI: https://doi.org/10.21203/rs.3.rs-10425660/v2

License: This work is licensed under a Creative Commons Attribution 4.0 International License.
Read Full License

Additional Declarations: No competing interests reported.

Title: Mouse genetic mosaic model for basal-like breast cancer reveals disruption of basal-myoepithelial architecture at premalignancy

Authors: Alexys T. Riddick[1#], Xian Zhou[2], Kevin A Janes[3], Hui Zong[1,2,#]

[1] Department of Pathology, University of Virginia, Charlottesville, VA 22908, USA.
[2] Department of Microbiology, Immunology, and Cancer Biology, University of Virginia, Charlottesville, VA 22908, USA.
[3] Department of Biomedical Engineering, University of Virginia, Charlottesville, VA 22908, USA
[#] Author for correspondence (hz9s@virginia.edu; atr8f@virginia.edu)
ORCID: A.R., 0000-0001-7803-0945; K.A.J., 0000-0002-8028-6138; H.Z., 0000-0002-4263-9633

Keywords: basal-like breast cancer, premalignancy, basal-myoepithelial architecture, whole-mount imaging, mouse genetic mosaic model

Abstract: In early cancer evolution, mutant cells must escape tissue-architectural constraints before progressing to malignancy. For invasive breast cancers, integrity of the wildtype basal-myoepithelial layer that wraps around premalignant luminal cells is lost before the formation of an invasive tumor mass. The spatiotemporal details of these early events have remained elusive. Here, we used a Mosaic Analysis with Double Markers (MADM) mouse model of basal-like breast cancer to generate rare, GFP-labeled, premalignant luminal cells within an otherwise normal mouse and pinpointed ductal hyperalveolarization as a key phase of progression, several months before malignant transformation. Using a whole-mount tissue clearing-staining-imaging workflow to examine the colorless basal-myoepithelial cell layer that surrounds GFP-labeled premalignant luminal cells, we observed a gradual disruption of the basal-myoepithelial layer during the hyperalveolarization phase. Increased cell size, altered cell morphology, and elevated proliferation of mutant cells occurred independently of basal disruption. In contrast, expression of the basal marker Keratin 14 in premalignant luminal cells, a feature that contributes to the “basal-like” nomenclature of this cancer, was strongly associated with basal disruption, suggesting that basal cell-mediated containment may suppress a critical transition in premalignant cell state. This work identifies disruption of the basal cell layer as an early hallmark of premalignant progression, supporting a chronology in which architectural remodeling of the mammary epithelium precedes malignant progression.

Statements and Declarations: The authors have no relevant financial or non-financial interests to disclose.

Acknowledgements: We thank Dr. Colinda Scheele for proofreading the manuscript. We also thank Marta Ciwinska for consulting on whole-mount tissue clearing and staining and Jeffrey Hsu for consulting on image data analysis. We thank Dr. Ying Jiang, Dr. Wenjie Liu, Dr. Piotr Przanowski and Arthur Huang for providing critical feedback on the manuscript figures. We also thank Dr. Sijie Hao at the Advanced Microscopy Core for assistance with the Imaris image analysis software and Hope Davis in the vivarium for management of the animal facilities.

Funding: This work was funded by the National Cancer Institute (R01-CA256199 to H.Z. and K.A.J.; R21-CA297427 to H.Z.), a UVA Cancer Center Grant (P30-CA044579 to H.Z. and A.R.), and a UVA Cancer Training Grant (T32-CA009109 to A.R.).

Author Contributions: Conceptualization: A.R., H.Z.; Methodology: A.R., X.Z.; Formal analysis: A.R.; Investigation: A.R., X.Z.; Writing - original draft: A.R., H.Z.; Writing - review & editing: A.R., X.Z., K.A.J., H.Z.; Visualization: A.R.; Supervision: K.A.J., H.Z.; Project administration: H.Z.; Funding acquisition: K.A.J., H.Z.

Introduction

Progression from premalignancy to malignancy is a multistep process. In addition to acquiring cell-intrinsic genetic alterations, premalignant cells must overcome tissue-level constraints that suppress tumor formation. The interplay between molecular and cellular tumor-suppressive mechanisms creates a selective environment in which only a minority of premalignant cells ultimately progress to cancer. Detailed studies of these rare events may shed light on novel early detection and cancer prevention strategies.

For basal-like breast cancer (BLBC), loss of *BRCA1* and *TP53* function represents an early genetic event in tumor initiation [1-6]. Despite their characteristic expression of basal cytokeratins, BRCA1-associated basal-like tumors originate from luminal epithelial progenitors [1, 2, 7-9], establishing altered luminal cell fate as an early component of BRCA1-associated tumorigenesis. In the normal mammary gland, luminal epithelial cells are surrounded by an outer basal-myoepithelial cell layer that regulates their differentiation and constrains their expansion [10-15]. For example, the basal-specific adhesion molecule P-cadherin restricts luminal cell proliferation and alveolar differentiation, and its loss results in excessive luminal proliferation and precocious alveolar development in virgin mice [16]. Experimental studies have further demonstrated that basal-myoepithelial cells can suppress tumor cell growth and dissemination [17-28]. In three-dimensional *in vitro* organotypic co-cultures, myoepithelial cells actively restrain and recapture invasive luminal cells, with barrier function depending on myoepithelial cell abundance, α-smooth muscle actin, and P-cadherin [22, 26]. During the transition from *in situ* to invasive disease, however, this barrier becomes compromised as tumor cells breach the myoepithelial layer and gain direct access to the surrounding microenvironment [29, 30]. To investigate changes in the basal-myoepithelial compartment before invasion, studies of breast tissue from *BRCA1* mutation carriers and patients with ductal carcinoma *in situ* identified disruption of the TP63- and TCF7-regulated transcriptional program required for normal myoepithelial differentiation, implicating dysfunction of this compartment before invasive breast cancer develops [31]. However, when and how basal-myoepithelial architecture becomes disrupted during premalignant progression remain unknown.

Investigating disruptions in native precancerous tissue architecture requires unequivocal visualization of rare premalignant cells *in vivo* and a comprehensive assessment of subtle changes in both premalignant lesions and their surrounding environment. For the former, we previously established a mouse model of BLBC using Mosaic Analysis with Double Markers (MADM-BLBC) [32], which generates rare GFP-labeled, *Brca1*,*Trp53*-null luminal cells within an otherwise normal mammary gland (**Supp 1A-B**). Previous studies used MADM-BLBC to identify expansion of mutant ductal cells and progressive morphological changes before tumor formation, relying primarily on traditional histological techniques to characterize changes within mutant luminal cells. Here, we extend previous work by combining MADM-BLBC with a tissue clearing and imaging protocol that is compatible with immunofluorescent staining and whole-mount, high-resolution imaging of the entire mammary gland [33, 34]. This approach enabled joint assessment of mutant luminal cells and the surrounding, genetically unaltered basal-myoepithelial layer, which identified early signs of basal architecture disruption associated with luminal cell plasticity before overt transformation.

Results

MADM-BLBC model reveals premalignant and early transformation phases prior to palpable tumor formation.

We backcrossed the initially mixed background of MADM-BLBC to a pure FVB/NJ background, which improves tumor penetrance with a relatively consistent latency [35]. This model also retains the rarity and permanent labeling of mutant cells, permitting high-resolution analysis of premalignant cells immediately following mutation acquisition (**Supp 1C**). Although MMTV-Cre was shown to mediate recombination in both luminal and basal-myoepithelial cells in conventional mouse models when loxP sites are on the same chromosome (in *cis*), we found that MMTV-Cre mediated recombination in MADM occurred exclusively within the luminal compartment, likely because loxP sites are on different chromosomes (in *trans*) and thus require high Cre for recombination to occur [32, 36]. Importantly, during pubertal expansion, the G2-phase requirement for MADM labeling (**Supp 1A**) restricts mutant cell generation to rapidly proliferating luminal progenitors, which are known to be the cell of origin for BLBC [1, 2, 8, 13, 37]. We validated recombination specificity by staining glands from 2-month-old MADM-BLBC mice for the luminal cell marker E-Cadherin (ECAD), and the basal cell marker Keratin 14 (K14), confirming that all GFP-labeled cells were ECAD positive and K14 negative (**Figure 1A,B**). After confirming their luminal cell origin, we next assessed the resulting tumors for an invasive phenotype by the loss of basal-myoepithelial cells and luminal cell plasticity by the gained expression of K14 [26, 27, 38-41]. Palpable tumors (arising at ~7 months) exhibited all these features in the GFP^+ tumor mass (**Figure 1C,D**). Together, these findings establish the beginning and endpoint of tumorigenesis in the MADM-BLBC model, providing bookends to investigate intermediate events during premalignant progression from luminal cell initiation to basal-like breast cancer formation.

To define the earliest phases of premalignant progression, we performed a time course analysis of the expansive patterns of GFP^+ lesions before the formation of palpable tumors by using whole-mount three-dimensional imaging. We harvested MADM-BLBC mice between 3 and 6 months of age, along with MADM-WT mice harvested at 6 months as a control, and used a three-dimensional clearing-staining-imaging workflow to quantify size differences between GFP^+ lesions in MADM-WT and MADM-BLBC mice (**Supp 1D-E**). At low magnification, we observed a gross increase in GFP^+ lesion abundance with age (**Figure 1E**). Volumetric analysis of contiguous GFP^+ lesions, presumably mutant clones, showed that, at 3 months, the size distribution of mutant lesions in MADM-BLBC mice were comparable in size to that of GFP^+ wild-type ducts in MADM-WT mice (**Figure 1F**). However, by 4-5 months, the volume of large lesions increased significantly and continued to grow by 6 months (**Figure 1F**). Interestingly, large premalignancies represented only a small fraction of all GFP^+ lesions: most remained small, suggesting that premalignant lesions are largely constrained.

To quantify morphological changes during lesion growth, we acquired high-resolution whole-mount images. 3-month-old MADM-BLBC and MADM-WT mice exhibited discrete stretches of GFP^+ ducts with occasional alveolar budding from ducts as seen during estrous cycles in virgin females (**Figure 1G**) [33, 42], suggesting that mutant cell expansion initially is restricted within the mammary ducts [32]. We asked whether this early mutant ductal expansion resulted in increased branching of mammary ducts at 3 months old by comparing the absolute number and frequency of primary, secondary and tertiary side branches in MADM-WT and MADM-BLBC mice. We found that the total number of branches, and the degree of side branching was increased in MADM-BLBC glands (**Supp 2A**), representing an early morphological distinction in mutant ductal expansion. By 4-5 months, GFP^+ lesions developed numerous alveolar buds beyond those expected from estrous cycling, forming hyperalveolar lesions on a hyper-branched ductal tree (**Figure 1G**), which represents a key morphological phase in premalignant progression [9, 32]. At 6 months, small masses lacking recognizable ductal or alveolar architecture emerged, likely indicating early transformation (**Figure 1G**). As mice aged,

simple duct lesions remained the predominant morphological phase at all ages, whereas rare hyperalveolar and early-transformed lesions became increasingly frequent in older MADM-BLBC mice (**Figure 1H**). Together, these findings define distinct phases of premalignant progression and indicate that the hyperalveolar lesion represents a critical point at which a subset of mutant luminal cells escape normal growth constraints, prompting investigation into the intracellular and tissue-level changes that accompany this transition.

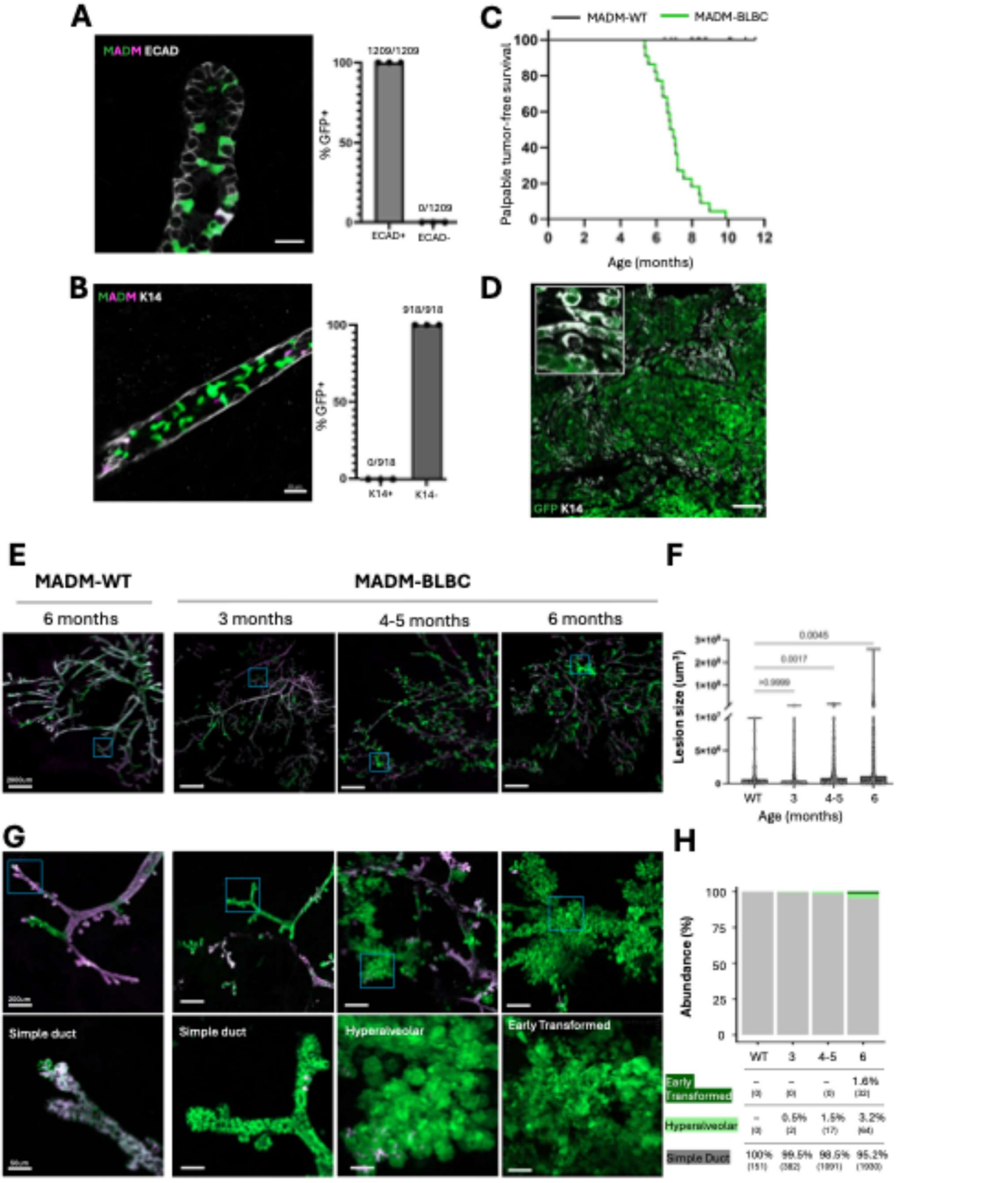
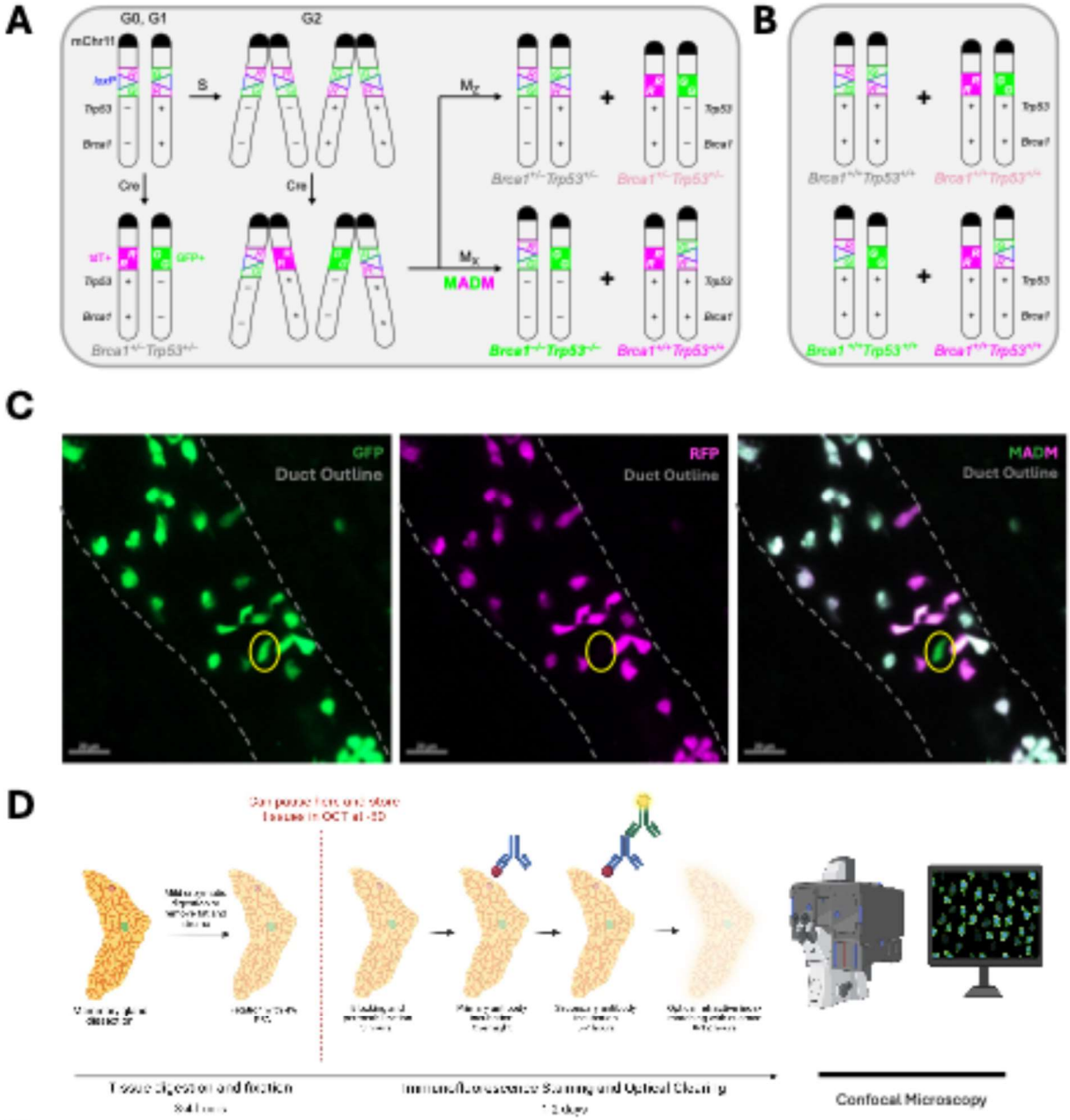
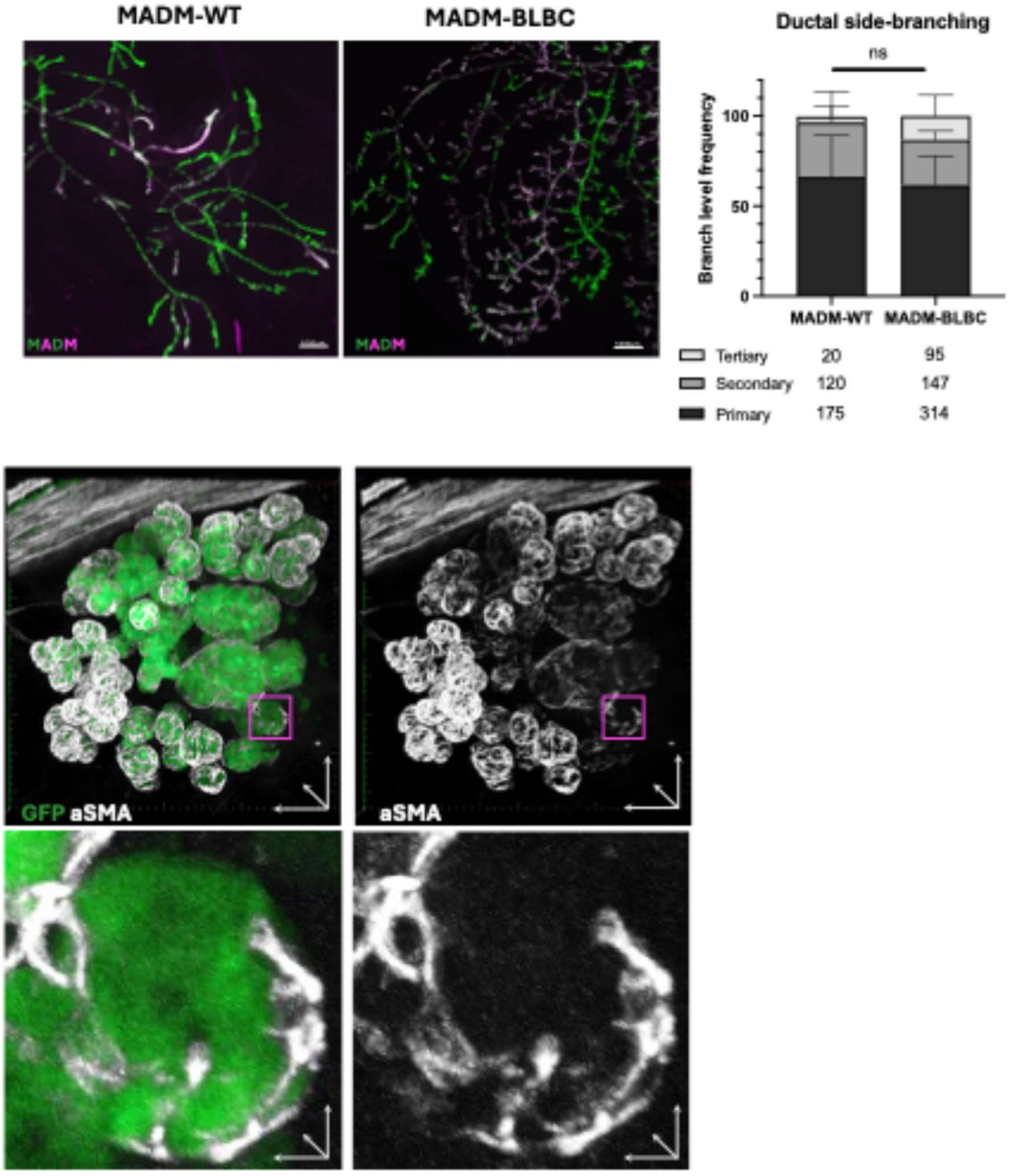

A
MADM ECAD
1209/1209
0/1209
% GFP+
ECAD+
ECAD-
B
MADM K14
918/918
0/918
K14+
K14-
C
MADM-WT
MADM-BLBC
Palpable tumor-free survival
Age (months)
D
GFP K14
E
MADM-WT
MADM-BLBC
6 months
3 months
4-5 months
6 months
F
Lesion size (um²)
0.0045
0.0017
>0.9999
WT
3
4-5
6
Age (months)
G
Simple duct
Simple duct
Hyperalveolar
Early Transformed
H
Abundance (%)
WT
3
4-5
6
Early Transformed
Hyperalveolar
Simple Duct
1.6%
0.5%
1.5%
3.2%
100%
99.5%
98.5%
95.2%

Fig 1. MADM-BLBC model reveals premalignant and early transformation phases prior to palpable tumor formation. (A) Representative image of 8-week-old MADM-BLBC mammary gland stained with E-cadherin (ECAD). Scale bar = 20um. Quantification across N=3 mice. **(B)** Representative image of mammary 8-week-old MADM-BLBC mammary gland stained with Keratin 14 (K14). Scale bar = 20um. Quantification across N=3 mice. **(C)** Palpable-tumor free survival of MADM-WT and MADM-BLBC mice. N=14 MADM-WT mice; N=22 MADM-BLBC mice. **(D)** K14 staining in palpable GFP^+ MADM-BLBC tumors. Scale bar = 100um. **(E)** Whole mount tiled images of representative mammary glands at multiple ages prior to palpable tumor formation. Scale: x = 13.23mm, y = 13.23mm , z = 90um. **(F)** Lesion size quantification from whole mount images at each age. N=3-5 mice per age. Kruskal Wallis test. **(G)** Top row: Higher magnification tiled images of inset blue box from (E). Scale: x = 1.41mm, y = 1.41mm, z = 36um; Bottom row: Single field-of-view images of inset blue box from top row. Scale: x = 319.45um, y = 319.45um, z = 36um. The associated phase is written on each image. **(H)** Abundance of premalignant phases at each age using whole-mount image data from (F). Each phase is defined by lesion volume and morphology: Simple duct (less than $1e+07um^3$; 0-5 alveolar buds), Hyperalveolar (between $1e+07um^3$ and $2e+07um^3$; >5 alveolar buds), Early transformed (greater than $2e+07um^3$, no identifiable ducts or alveolar buds). The absolute number and percentage of lesions classified as each phase is written below the associated age. N=3-5 mice per age.


A
G0, G1
G2
mChr11
loxP
Trp53
Brca1
S
Cre
Cre
Mc
Mx
MADM
Brca1+/-Trp53+/-
Brca1-/-Trp53-/-
Brca1+/+Trp53+/+
B
C
GFP
Duct Outline
RFP
Duct Outline
MADM
Duct Outline
D
Confocal Microscopy
E
MADM
Imaris GFP mask

Supplement 1. (A) Schematic of MADM's Cre-loxP-mediated interchromosomal mitotic recombination for MADM, *Brca1,Trp53; MMTV-Cre* mice. The alleles for the MADM cassettes, *Trp53KO* and *Brca1*$^{fl/fl}$ are located on mouse chromosome 11 (mChr11). From a colorless heterozygous cell, MMTV-Cre-mediated inter-chromosomal recombination during G2 produces one GFP$^+$ *Brca1,Trp53*-mutant cell and one RFP$^+$ (pseudocolor magenta) wild-type cell after X segregation, when recombinant sister chromatids segregate into different daughter cells. Alternatively, Z segregation yields one colorless and dual-labeled GFP$^+$RFP$^+$ heterozygous cell when recombinant sister chromatids segregate into the same daughter cell. More frequently, recombination occurs in colorless heterozygous cells without DNA replication (G0/G1), producing abundant dual-labeled heterozygous cells (shown on far left). **(B)** Schematic representation of cells produced within MADM wildtype mice, without any mutations. **(C)** MADM endogenous fluorescence in 3-week-old MADM-BLBC mice. Single channel and merged images of GFP (green) and RFP (magenta). Yellow circle denotes single *BRCA1,Trp53*-mutant cell. Scale bar = 20um. **(D)** Schematic of whole mount mammary gland clearing-staining-imaging workflow. **(E)** Whole mount image from MADM-WT Figure 1E, processed using Imaris to mask GFP$^+$ lesions.



Supplement 2. (A) Whole mount images of mammary glands from 3-month-old MADM-WT and MADM-BLBC mice. Quantification of the frequency of primary, secondary or tertiary side branches from the main duct. N=3 mice with one mammary gland quantified per mouse. T-test on arcsine square root transform of percentage. Absolute number of total ducts from N=3 mice below the graph. **(B)** Representative image of basal-myoepithelial cell disorganization in fresh fixed mammary gland tissue without enzymatic digestion. Left: 3D projection of αSMA staining and GFP. Scale: x = 424.26um, y = 424.26um, z = 45um. Right: 3D projection of αSMA staining. Scale: x = 424.26um, y = 424.26um, z = 45um. Bottom: Scale: x = 50um, y = 50um, z = 45um.

Basal-like breast cancer hallmarks arise at the hyperalveolar premalignant phase.

We next investigated the evolution of luminal cell-intrinsic features of basal-like tumors during premalignant progression, paying close attention to significant changes at the hyperalveolar phase. Since basal-like tumor cells have pleomorphic morphology and a high mitotic index [26], we used the luminal cell-specific membrane protein E-cadherin to assess cell size and circularity and Ki67 to detect proliferation in ductal, hyperalveolar, and early-transformed lesions. Individual cell size was comparable between MADM-WT (GFP^+RFP^+ appear yellow) and MADM-BLBC (GFP^+ only) simple ducts, but increased significantly in hyperalveolar lesions and even further in early-transformed lesions (**Figure 2A,B**). Cell circularity progressively decreased from the hyperalveolar phase onward, indicating increased irregularity of cell morphology (**Figure 2A,C**). Lastly, we found that proliferation significantly increased at the hyperalveolar phase and continued to progress at the early-transformed phase (**Figure 2D,E).** Together, these data show that *Brca1,Trp53*-mutant cells overall become larger, more irregular in shape, and more proliferative at the hyperalveolar phase. The changes prompted us to ask whether hyperalveolarization is also accompanied by acquisition of the defining lineage features of basal-like tumors.

The most unique feature of basal-like tumors is the expression of basal cytokeratins on luminal cells, indicative of lineage plasticity that contributes to malignancy [2, 26, 38-41]. MADM-BLBC initiates from $K14^-$ luminal cells yet forms GFP^+ tumors comprised of cells that are $K14^+$ (**Figure 1B,D**), prompting the question of when and where K14 misexpression starts during premalignant progression. At the hyperalveolar phase, we found that $K14^+GFP^+$ cells emerged sporadically and increased in abundance at the early-transformed phase (**Figure 2F,G**). Notably, these $K14^+$ cells at premalignancy and early transformed phases were still $ECAD^+$, implying that they still retained some of their luminal identity (**Figure 2F**). Thus, luminal cell misexpression of basal cytokeratin is an early event that occurs before overt transformation. Taken together, these data demonstrate that hallmarks of basal-like breast cancer—increased proliferation, altered cell morphology, and acquisition of basal cytokeratin expression—first emerge heterogeneously at the hyperalveolar phase and increase during early transformation.

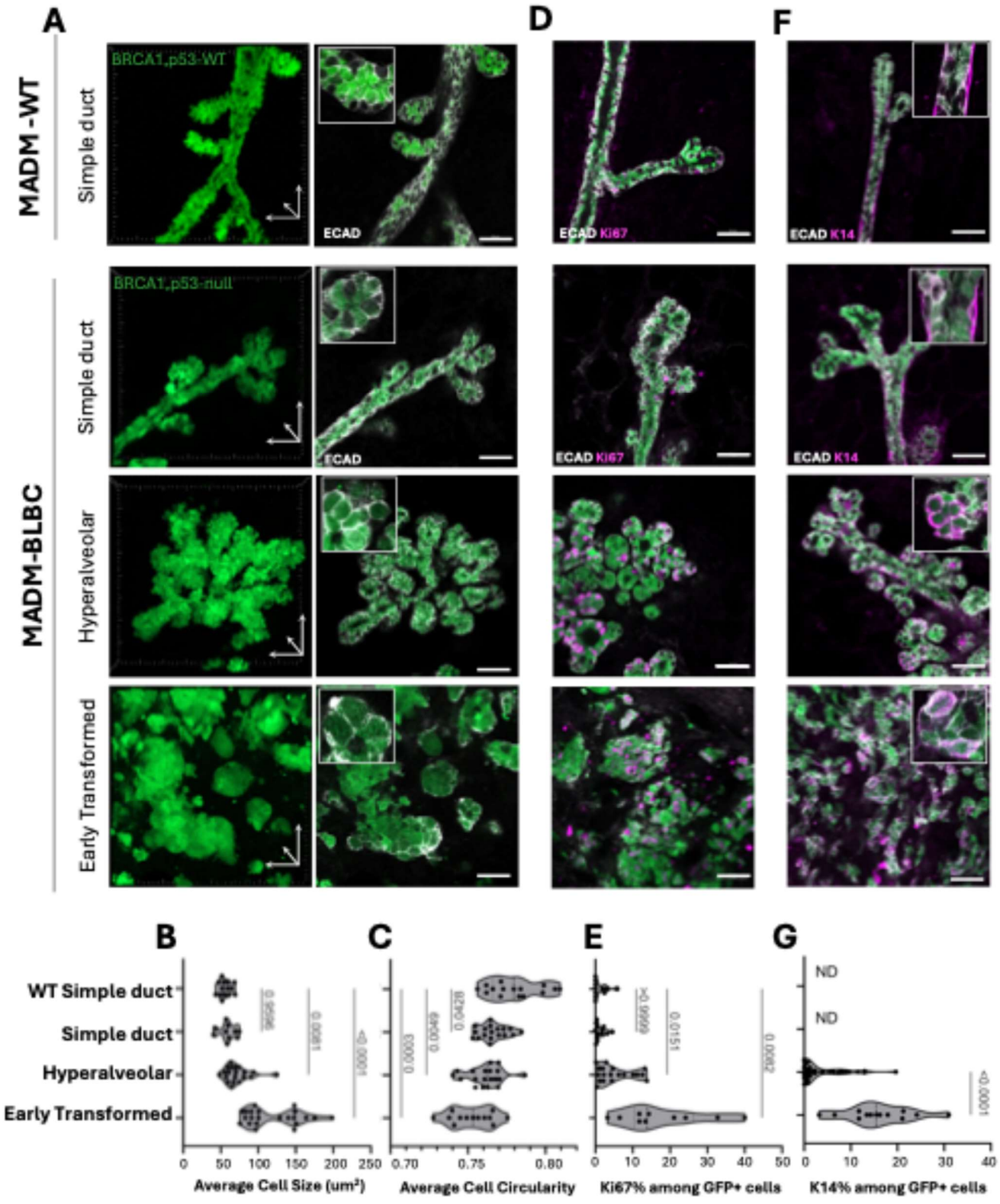

A
D
F
MADM-WT
Simple duct
BRCA1,p53-WT
ECAD
ECAD Ki67
ECAD K14
MADM-BLBC
Simple duct
BRCA1,p53-null
Hyperalveolar
Early Transformed
B
C
E
G
WT Simple duct
Simple duct
Hyperalveolar
Early Transformed
0.9596
0.0361
<0.0001
0.0003
0.0049
0.0428
>0.9999
0.0151
0.0002
ND
ND
<0.0001
0 50 100 150 200 250
Average Cell Size (um²)
0.70 0.75 0.80
Average Cell Circularity
0 10 20 30 40 50
Ki67% among GFP+ cells
0 10 20 30 40
K14% among GFP+ cells

Fig 2. Basal-like breast cancer hallmarks arise at the hyperalveolar premalignant phase. (A) Left column: 3D projection of simple ducts, hyperalveolar and early transformed lesions. Scale: x = 319.45um, y = 319.45um, z = 36um; Right column: Optical cross-section with E-cadherin (ECAD) staining. Scale bar = 50um. Quantification in (B-C). **(B)** Quantification of the average cell size within each lesion. Cell size was averaged from over 1000 cells per lesion. N=3-5 mice per phase, with 2-5 lesions quantified per mouse. Welch's ANOVA with Dunnett's T3 post-hoc test. **(C)** Quantification of the average cell circularity within each lesion. Cell circularity was averaged from over 1000 cells per lesion. N=3-5 mice per phase, with 2-5 lesions quantified per mouse. Welch's ANOVA with Dunnett's T3 post-hoc test. **(D)** Optical cross-section of lesions with ECAD and Ki67 staining. Scale bar = 50um. Quantification in (E). **(E)** Quantification of Ki67 percentage per lesion at each phase. N=3-5 mice per phase, with 2-5 lesions quantified per mouse. Welch's ANOVA with Dunnett's T3 post-hoc test. **(F)** Optical cross-section of lesions with ECAD and Keratin 14 (K14) staining. Scale bar = 50um. Quantification in (G). **(G)** Quantification of K14 percentage among GFP^+ cells in lesions at each phase. N=3-5 mice per phase, with 2-5 lesions quantified per mouse. ND = not detected. Welch's t-test.

Basal-myoepithelial architecture disruption emerges heterogeneously at the hyperalveolar phase.

Since the hyperalveolar phase marks a critical cellular transition during premalignant progression, we next asked whether it is accompanied by changes in the surrounding basal-myoepithelial layer, a tissue-level tumor suppressor that normally constrains luminal cell behavior [18, 22, 43]. Whole-mount immunofluorescence for α-smooth muscle actin was used to visualize the entire basal-myoepithelial layer. As expected, basal-myoepithelial cells were aligned parallel to simple luminal ducts [44] and were largely absent in early transformed lesions (**Figure 3A,B**). Interestingly, before overt transformation, a rare subset of hyperalveolar lesions exhibited morphological changes to the basal-myoepithelial cells, where they no longer fully encapsulated the GFP^+ cells (**Figure 3A,B**). Together, these observations suggest that organizational changes within the basal-myoepithelial cell layer are not absolutely required for hyperalveolar lesion formation itself; rather, it is likely a later event occurring within a small subset of these lesions.

Basal-myoepithelial cells are anchored between luminal cells and the basement membrane they produce [45, 46]. We therefore asked whether organizational changes in basal-myoepithelial cells were also reflected in the basement membrane. When staining for the basement membrane proteins laminin-1 (**Figure 3C**) and collagen IV (**Figure 3D**), we found that their organization was also disrupted with basal-myoepithelial cells. In intact lesions, we found the basement membrane formed an aligned layer outside of the basal-myoepithelial cells. However, in disrupted lesions, the normal organizational pattern was distorted (**Figure 3C-D**). This phenotype indicates that organizational disruption occurs in both the basal-myoepithelial and basement membrane layers in a subset of hyperalveolar lesions.

Lastly, we asked whether distortion of the basal-myoepithelial layer occurred abruptly or through a gradual process at the hyperalveolar phase. Our analysis of 23 hyperalveolar lesions with basal disruption revealed some partial disruption where less than half of the GFP^+ lesion lacked organized basal-myoepithelial cells, and other broad disruptions where most of the lesion lacked an organized basal cell layer (**Figure 3E-F**), suggesting that this phenotype likely develops focally. Together, these findings demonstrate that organizational changes in the basal-myoepithelial cell layer and basement membrane emerge gradually and stochastically in a rare subset of hyperalveolar lesions during premalignant progression, suggesting that tissue-level containment is breached before overt malignancy.

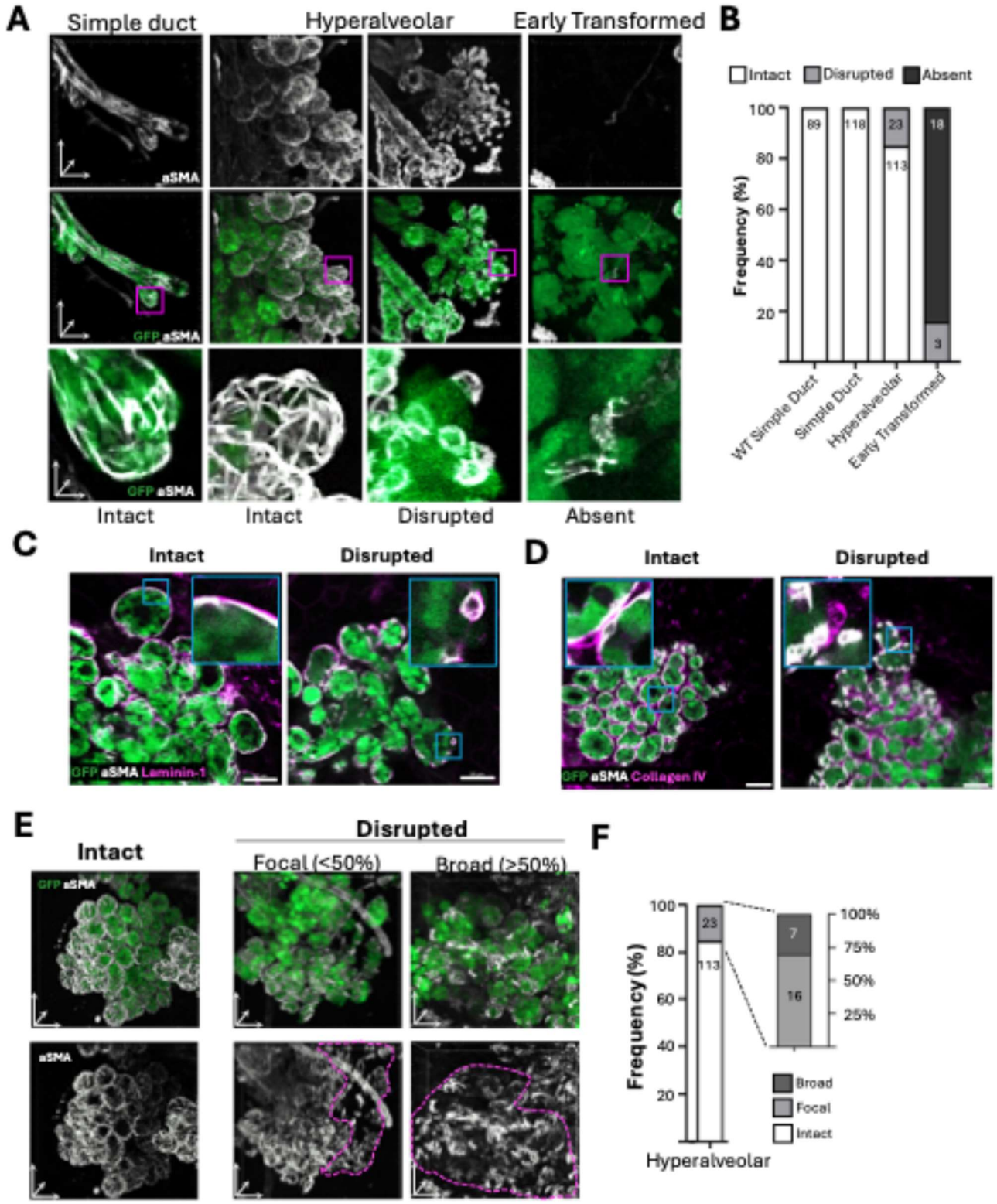

A
Simple duct
Hyperalveolar
Early Transformed
aSMA
GFP aSMA
GFP aSMA
Intact
Intact
Disrupted
Absent
B
Intact
Disrupted
Absent
Frequency (%)
100
80
60
40
20
89
118
23
113
18
3
WT Simple Duct
Simple Duct
Hyperalveolar
Early Transformed
C
Intact
Disrupted
GFP aSMA Laminin-1
D
Intact
Disrupted
GFP aSMA Collagen IV
E
Intact
Disrupted
Focal (<50%)
Broad (≥50%)
GFP aSMA
aSMA
F
Frequency (%)
100
80
60
40
20
23
113
7
16
100%
75%
50%
25%
Broad
Focal
Intact
Hyperalveolar

Fig 3. Basal-myoepithelial architecture disruption emerges heterogeneously at the hyperalveolar phase. (A) Top row: 3D projection of α-smooth muscle actin staining (αSMA) around simple ducts, hyperalveolar and early transformed lesions. Scale: x = 319.45um, y = 319.45um, z = 36um; Middle row: 3D projection of αSMA staining with GFP. Scale: x = 319.45um, y = 319.45um, z = 36um; Bottom row: Zoom in of αSMA staining around one GFP^+ alveolar bud from magenta box in middle row. Scale: x = 50um, y = 50um, z = 36um. Quantification in (B). Note: αSMA labels endothelial vasculature in early transformed lesions. **(B)** Frequency of intact, disrupted or absent basal architecture at each phase measured from 15-100 lesions. N= 4-7 mice per phase, with more than 3 lesions counted per mouse. **(C)** Representative images of Laminin and αSMA staining in hyperalveolar lesions with intact (left) and disrupted (right) basal architecture. Scale bar = 50um. **(D)** Representative images of Collagen IV and αSMA staining in hyperalveolar lesions with intact (left) and disrupted (right) basal architecture. Scale bar = 50um. **(E)** Top row: 3D projection of hyperalveolar and early transformed lesions with degrees of basal architecture disruption. Scale: x = 319.45um, y = 319.45um, z = 36um; Bottom row: 3D projection of αSMA staining. Scale: x = 319.45um, y = 319.45um, z = 36um. Pink dashed line outlines disrupted region. Quantification in (F). **(F)** Frequency of intact, focal, or broad disruption in the hyperalveolar phase measured from ~150 lesions. N=4-7 mice, with more than 10 lesions counted per mouse.

Basal architecture disruption correlates with luminal cell misexpression of Keratin 14.

Finally, we sought to determine how the disorganization of the basal-myoepithelial layer correlates with luminal cell-intrinsic features of premalignant progression. Because broad basal disorganization was infrequent, focal and broad disruption categories were combined for subsequent analyses. We quantified lesion volume, proliferation, individual GFP^+ cell size and circularity, and K14 misexpression in hyperalveolar lesions with or without disrupted basal architecture.

To determine whether basal disruption was associated with luminal cell growth during premalignant expansion, we compared lesion size and proliferation between hyperalveolar lesions with intact and disrupted basal architectures. We found that the lesion volume distribution was unaltered in disrupted lesions, nor were disrupted lesions significantly more proliferative (**Figure 4A-C**). Similarly, individual GFP^+ cell size and circularity were also comparable between lesions with intact and disrupted architecture (**Figure 4A,D-E**). These data suggest that physical forces generated by luminal cell outgrowth, rapid proliferation, or pronounced morphological abnormalities do not explain basal architecture disorganization, plausibly distinguishing this phenotype as a distinct biological transition during progression.

In contrast, however, K14-misexpressed GFP^+ luminal cells were significantly more abundant in a subset of hyperalveolar lesions with disrupted GFP^- basal architecture (**Figure 4F-G**), implying greater cell plasticity in response to basal layer disruption. We asked whether there was a spatial correlation between basal disruption and luminal cell plasticity. Taking advantage of focally disrupted lesions that contain both intact and disrupted areas, we quantified the number of $K14^+$ GFP^+ cells near the intact or focally disrupted areas within the same hyperalveolar lesions and noticed an enrichment in the number of $K14^+$ premalignant cells adjacent to the focally disrupted regions of the basal layer (**Figure 4H-I**). This finding implies a relationship between basal disruption and K14 misexpression in mutant luminal cells: either luminal cell plasticity is promoted in response to basal layer disruption at a focal level, or luminal cell plasticity promotes basal disruption. The former could be caused by altered environmental cues that luminal cells are now exposed to upon the disruption of basal cell organization [47], while the latter could be caused by altered paracrine signals from K14-misexpressed mutant luminal cells leading to the loss of basal layer integrity [31]. Additionally, these processes could form a positive feedback and mutually promote each other. Taken together, among all luminal features examined, K14 abundance was the only feature significantly correlated with basal architecture disruption, uniquely associating basal layer disruption with luminal cell plasticity.

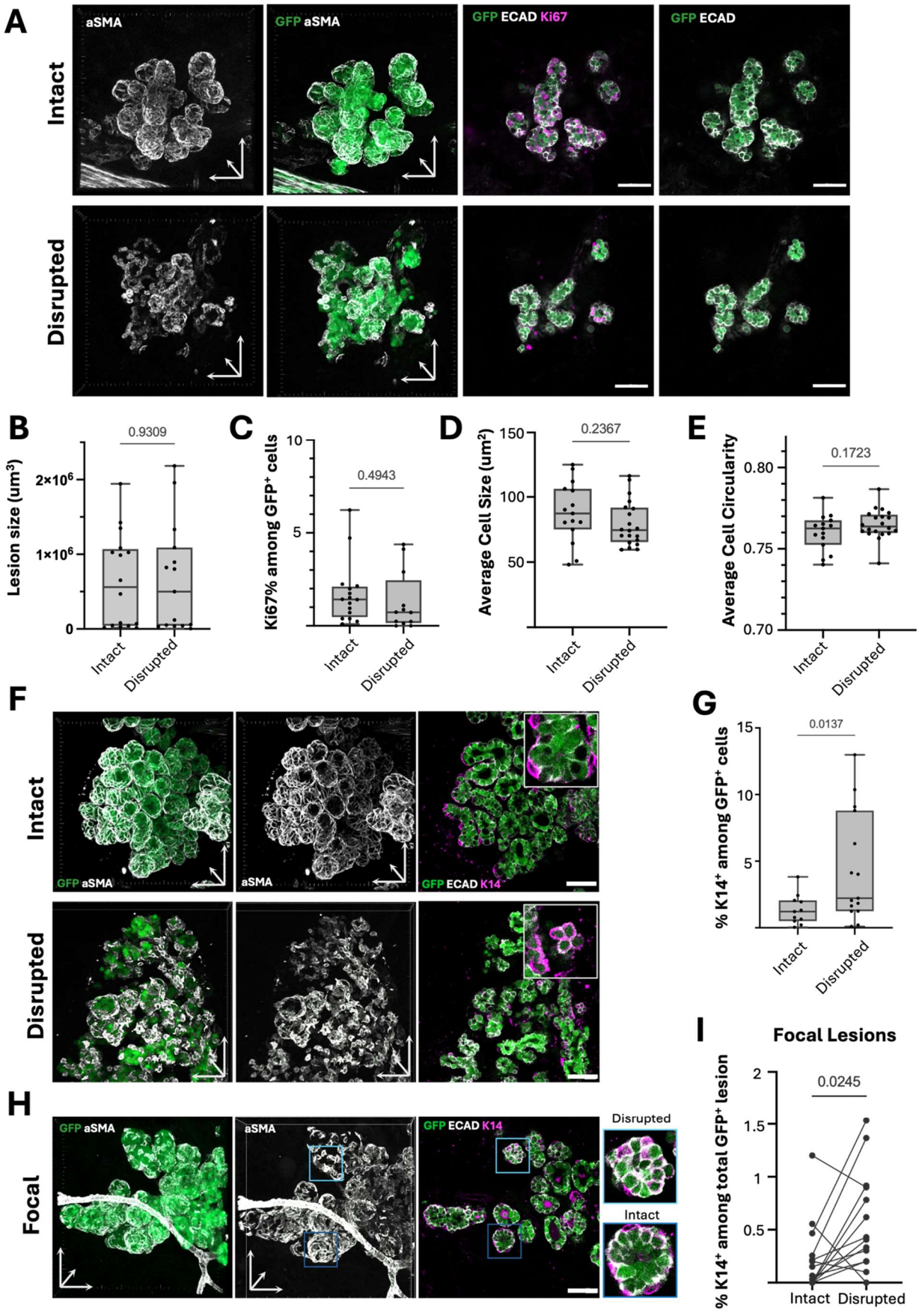

A
aSMA
GFP aSMA
GFP ECAD Ki67
GFP ECAD
Intact
Disrupted
B
Lesion size (um³)
0.9309
C
Ki67% among GFP⁺ cells
0.4943
D
Average Cell Size (um²)
0.2367
E
Average Cell Circularity
0.1723
F
GFP aSMA
aSMA
GFP ECAD K14
G
% K14⁺ among GFP⁺ cells
0.0137
H
Focal
I
Focal Lesions
% K14⁺ among total GFP⁺ lesion
0.0245

Fig 4. Basal architecture disruption correlates with luminal cell expression of Keratin 14. (A) Far left: 3D projection of αSMA staining. Scale: x = 319.45um, y = 319.45um, z = 36um; Middle left: 3D projection of hyperalveolar lesions with GFP and a-smooth muscle actin (αSMA) staining. Scale: x = 319.45um, y = 319.45um, z = 36um. Quantification in (B); Middle right: Optical cross-section with E-cadherin (ECAD) and Ki67 staining. Scale bar = 50um. Quantification in (C); Far right: Optical cross-section with ECAD staining. Scale bar = 50um. Quantification in (D-E). **(B)** Quantification of hyperalveolar lesion size with varying degrees of basal architecture disruption. N=3-5 mice, with 2-5 lesions quantified per mouse. Welch's t-test. **(C)** Quantification of Ki67 percentage within hyperalveolar lesions with intact or disrupted basal architecture. N= 3-4 mice, with 2-5 lesions quantified per mouse. Welch's t-test. **(D)** Quantification of the average cell size within hyperalveolar lesions with intact or disrupted basal architecture. Cell size was averaged from over 1000 cells per lesion. N=3-5 mice, with 2-5 lesions quantified per mouse. Welch's t-test. **(E)** Quantification of the average cell circularity within hyperalveolar lesions with intact or disrupted basal architecture. Cell circularity was averaged from over 1000 cells per lesion. N=3-5 mice, with 2-5 lesions quantified per mouse. Welch's t-test. **(F)** Left: 3D projection of hyperalveolar lesions with GFP and αSMA staining. Scale: x = 319.45um, y = 319.45um, z = 36um; Middle: 3D projection of αSMA staining. Scale: x = 319.45um, y = 319.45um, z = 36um; Right: Optical cross-section with E-Cadherin (ECAD) and Keratin 14 (K14) staining. Scale bar = 50um. Quantification in (G). **(G)** Quantification of K14 percentage among GFP^+ cells within hyperalveolar lesions with intact or disrupted basal architecture. N=3-5 mice, with 2-5 lesions quantified per mouse. Welch's t-test. **(H)** Left: 3D projection of hyperalveolar lesions with focal basal disruption. Scale: x = 319.45um, y = 319.45um, z = 36um; Middle: 3D projection of αSMA staining. Light blue square denotes disrupted area. Dark blue square denotes intact area. Scale: x = 319.45um, y = 319.45um, z = 36um; Right: Optical cross-section with ECAD and K14 staining. Scale bar = 50um. Light blue square denotes disrupted area. Dark blue square denotes intact area. Quantification in (I). **(I)** Quantification of K14% in focal disrupted lesions, where $K14^+$ GFP^+ luminal cells are binned by their location nearby either intact or disrupted portions of the same hyperalveolar lesion. N=3-5 mice, with 2-5 lesions quantified per mouse.

Discussion

In this study, we define key phases and tissue architecture alterations during premalignant progression in the MADM-BLBC mouse model. Although most *Brca1,Trp53*-mutant lesions remained as simple ducts, a rare subset progressed to the hyperalveolar phase, where hallmark features of basal-like breast cancer—including increased proliferation, altered cell morphology, and acquisition of basal cytokeratin expression—first emerged. Within this rare population, only a fraction exhibited disruption of the surrounding basal-myoepithelial architecture. Notably, basal architecture disruption uniquely associated with luminal K14 misexpression, but not with increased lesion size, proliferation, or pleomorphic morphology. Our work identifies disruption of the basal-myoepithelial layer as a previously unrecognized feature of premalignant progression that accompanies luminal cell plasticity.

To address the dynamic relationship between the basal-myoepithelial cell layer and premalignant luminal cells, we combined a lineage tracing tool with whole mount clearing, staining and imaging of the mammary fat pad. Our specific genetic mosaic mouse model is ideal for studying premalignant progression of BLBC because it mimics human cancer initiation by generating rare mutant cells in a mosaic fashion [36, 48] and phenocopies features found in BRCA carrier disease-free tissue, such as increased proliferation and basal cytokeratin misexpression [32, 49, 50]. Our previous study established that these mutant cells originate in the luminal compartment and undergo progressive ductal expansion and morphological changes before tumor formation [51]. Here, we extend this work beyond the mutant luminal compartment by examining the surrounding, genetically unaltered basal-myoepithelial layer. Coupling this model with tissue clearing techniques applicable for immunofluorescence staining of the mammary fat pad [33, 34, 52, 53] enabled high-throughput analyses of spatial interactions between GFP^+ premalignant luminal cells and colorless, bystanding basal-myoepithelial cells, which would be challenging to resolve with traditional histological techniques.

One central finding in this study was the identification of basal-architecture disruption before malignant transformation, arising in a subset of hyperalveolar lesions. Previous literature suggests a failure of basal-myoepithelial integrity contributes to invasiveness at the tumor stage [21, 22, 25]. Our findings demonstrate that before invasion, the basal layer is already compromised, complementing studies that identified altered myoepithelial differentiation and decreased myoepithelial cell abundance in disease-free tissue from BRCA carriers before invasive disease [31]. Ciwinska et. al. previously discovered geometric constraints as a tissue protection mechanism in the mammary gland that limits mutant clonal expansion using a model prediction of how premalignant ductal cells should expand over time [33]. While the modeling study did not specifically address the source of geometric constraints, our data suggests that basal-myoepithelial cells may be the cellular mediators of this geometric constraint. Although the basal-myoepithelial layer remains intact in most hyperalveolar lesions, focal disruptions may release the geometric constraint to permit further progression. The mechanism underlying basal disruption remains unresolved. While our study found that is it not simply a result of luminal cell expansion, further studies should determine whether disrupted regions reflect loss of basal-myoepithelial cells, altered cell organization, or an inability of the basal layer to accommodate luminal expansion.

We further identified a previously unappreciated association between basal-myoepithelial disruption and luminal cell-state plasticity. Among the different features tested in this study, only K14 misexpression in luminal cells increased with basal disruption. This suggests that increased proliferation and altered cell morphology occur in premalignant luminal cells even under basal layer constraint, and these phenotypes are not significantly altered upon basal layer disruption. While the same features are well attributed to cancer grade and stage [26], alone, they may not be indicative of the most high risk precancerous lesions. The correlation between basal disruption and K14 misexpression in the luminal compartment uniquely associates tissue architecture with luminal cell-state plasticity. Lineage plasticity is known to be activated in the mammary gland

by several inciting events, including oncogenic insult and environmental factors [38, 39, 41, 47, 54-57]. Our data show that luminal premalignant cell plasticity appears stochastically at the hyperalveolar phase. However, upon basal architecture disruption, premalignant luminal cells are more prone to K14 misexpression near the site of disruption, suggesting a combined effect of both intrinsic oncogenic changes and extrinsic environmental cues. Notably, these cells retain E-cadherin expression, supporting an altered luminal cell state rather than complete conversion to a basal lineage. Future studies are warranted to determine how basal disruption impacts luminal lineage plasticity, or vice versa, thereby paving a way forward to pinpoint opportunities for cancer prevention.

Several limitations should be considered when interpreting these findings. First, the whole-mount clearing-staining-imaging workflow includes brief enzymatic digestion, which is essential for antibody penetration and faithful immunofluorescence staining within mammary ducts, but could also alter cellular morphology or exaggerate pre-existing discontinuities in the basal-myoepithelial layer (**Supp 2B**) [58]. However, since all MADM-WT and MADM-BLBC tissues were processed using the same protocol, and basal disruption was restricted to a subset of hyperalveolar lesions rather than being broadly observed in wildtype glands or simple mutant ducts (**Figure 3B**), we can reasonably conclude that the disruption phenotype described here was not caused by digestion. Second, individual lesions could not be followed longitudinally to determine whether hyperalveolar lesions with disrupted basal architecture are those that ultimately transform, which would require *in vivo* identification of basal disruption. Finally, although basal disruption may represent an early feature of progression, its clinical value will depend on validation in human premalignant tissue and identification of accessible biomarkers associated with this architectural transition. Such studies may determine whether basal-myoepithelial disruption or its associated molecular changes might inform early detection and prevention strategies for BRCA1-associated breast cancer.

Methods

Animals

Briefly, stocks used to produce MADM-BLBC and MADM-WT were generated from the following mouse lines, as described in [32]: TG11ML (RRID:IMSR_JAX:022977), Brca1flox (RRID:MGI:3618507), p53KO (RRID:IMSR_JAX:002101), GT11ML (RRID:IMSR_JAX:022976) and MMTV-Cre (RRID:IMSR_JAX:003553). The resulting TG11ML,Brca1flox,p53KO stocks and GT11ML; MMTV-Cre stocks were backcrossed to FVB/NJ mice (RRID:IMSR_JAX:001800) for 6 generations and verified using speed congenics (RRID:SCR_009757) to reach >96% FVB similarity. All animal work was performed in the University of Virginia Animal Vivarium. All procedures, including housing and husbandry were approved by the Institutional Animal Care and Use Committee (IACUC) at the University of Virginia, following national guidelines to ensure the humanity of all animal experiments. Mice from multiple estrous cycles were pooled for data analyses.

Genotyping

Genotyping was performed as described in [32]. Briefly, the mouse toe was used to extract DNA for PCR. First, 120 µl of 50 mM NaOH was added to each toe and then incubated at 95°C for 20 min in the PCR machine, followed by addition of 30 µl of 1 M Tris-HCl (pH 7.4) and mixing. One microliter of the toe solution was used for the PCR template in a 20 µl PCR reaction. PCR primer sequences were as follows. (1) MADM TG/GT cassettes: primer-1, 5-TGGAGGAGGACAAACTGGTCAC-3; primer-2, 5-TCAATGGGCGGGGGTCGTT-3; primer-3, 5-TTCCCTTTCTGCTTCATCTTGC-3; PCR products, knock-in (KI) band, 230 bp and wild-type band, 350 bp. (2) MMTV-Cre: primer-1, 5-CACCCTGTTACGTATAGCCG-3; primer-2, 5-GAGTCATCCTTAGCGCCGTA-3; PCR product, KI band, 300 bp. (3) p53KO: primer-1, 5-ACCGCTATCAGGACATAGCGTT-GG-3; primer-2, 5-CACAGCGTGGTGGTACCTTATG-3; primer-3, 5-GGTATACTCAGAGCCGGCCTG-3; PCR products, KI band, 700 bp and wild-type band, 450 bp. (4) Brca1flox: primer-1, 5-CTGGGTAGTTTGTAAGCATCC-3, primer-2, 5-TCTTA-GCCCTCAGAAAACTC-3; PCR products, flox/flox band, 365 bp and wild-type band, 297 bp.

Whole-mount immunofluorescence staining of mammary glands

Whole-mount immunofluorescence staining was adapted from [33, 59]. The first, second and third mammary glands were dissected and incubated in a mixture of 2.5mg/mL collagenase type I (Thermo Fisher Scientific, Cat#: 17-100-017) and 10ug/mL hyaluronidase (Sigma-Aldrich, Product#: H3884) at 37°C for 20 minutes at 200 rpm, fixed in 4% PFA for 2 hours at room temperature, and incubated for at least 3 hours in blocking buffer containing 1% bovine serum albumin, 5% normal goat serum, 0.8% Triton X-100 and 0.01% sodium azide in PBS. Primary antibodies were diluted in blocking buffer and incubated overnight at 4°C. Glands were optically cleared using a supersaturated solution of 100g sucrose in 50mL ddH2O overnight at room temperature before being mounted on a microscopy slide using VectaShield Antifade mounting media (Vector Laboratories, Ref#: H1900). Another slide was used to press and flatten the mammary gland firmly before sealing with nail polish. Primary antibody used: Keratin 14 polyclonal antibody (1:100; BioLegend, Cat#: 905301, RRID:AB_2565048). Secondary antibodies used: Donkey anti-rabbit IgG AF555 (1:250; Jackson ImmunoResearch Labs Cat# 711-565-152, RRID:AB_3095471), Donkey anti-rabbit IgG AF647 (1:250; Jackson ImmunoResearch Labs Cat# 711-605-152, RRID:AB_2492288). Conjugated primary antibodies used: anti-E-Cadherin-BV421 (1:200; BioLegend, Cat#: 147319, RRID:AB_2750483), anti-Ki67-AF594 (1:200; Thermo Fisher Scientific, Cat#: 755-5698-94, RRID:AB_3679245), anti-Ki67-eFluor660 (1:200; Thermo Fisher Scientific, Cat#: 50-5698-82, RRID:AB_2574235), anti-α Smooth Muscle Actin (SMA)-AF647 (1:200; BioLegend, Cat#: 614856, RRID:AB_3662309).

Whole-mount imaging of mammary glands

Imaging of whole-mount mammary glands was performed using an inverted Zeiss LSM 900 confocal microscope, equipped with 405nm, 488nm, 561nm and 640nm lasers. Different fluorophores were excited as follows: BrilliantViolet-421 at 405nm, green fluorescent protein (GFP) at 488 nm, red fluorescent protein (RFP) and AlexaFluor-594 at 561 nm, and AlexaFluor-647 and eFluor-660 at 633 nm. BrilliantViolet-421 was collected at 410–470 nm, GFP was collected at 400–632 nm, RFP and AlexaFluor-594 at 400-650 nm, and AlexaFluor-647 and eFluor-660 at 636–700 nm. Whole mount images were acquired with an EC Plan-Neofluar 5x/0.16 DIC objective (Zeiss, Item#: 420331-9911-000) using a Z-step size of 30um (total Z-stack around 90um) spanning large tile-scan areas. Higher magnification tiled images were acquired with a Plan-Apochromat 10x/0.45 M27 objective (Zeiss, Item#: 420640-9900-000) using a Z-step size of 4um (total Z-stack around 36um) spanning 25 tiles. Detailed images of individual phases were obtained with a Plan-Apochromat 20x/0.8 M27 objective (Zeiss, Item#: 420650-9902-000) using a Z-step size of 4um (total Z-stack around 36um). All images were stitched and processed using ZEN 3.4 and further processed using IMARIS software.

Whole-mount image processing

Using Imaris 11.0, a surface was created using the Machine Learning module to mask and measure contiguous GFP^+ lesions in whole-mount images (**Supp 1D**). Data tables from Imaris were imported into R studio or GraphPad Prism to compose graphs. Single-cell segmentation masks of luminal epithelial cells were generated from individual ECAD z-stack immunofluorescence images using CellPose-SAM (CellPose v4.0.5). The resulting masks were imported into CellProfiler for downstream single-cell feature extraction, such as cell size, cell circularity, Ki67-positivity or K14-positivity. Data tables from CellProfiler were imported into R studio or GraphPad Prism to compose graphs.

Statistics

Statistical analysis was performed with GraphPad Prism. The normality of data distribution was checked with qqplot in R. P values and statistical tests performed are included in the figure legends.

References

1. Wang, H., et al., *Inadequate DNA Damage Repair Promotes Mammary Transdifferentiation, Leading to BRCA1 Breast Cancer.* Cell, 2019. **178**(1): p. 135-151.e19, https://dx.doi.org/10.1016/j.cell.2019.06.002
2. Molyneux, G., et al., *BRCA1 Basal-like Breast Cancers Originate from Luminal Epithelial Progenitors and Not from Basal Stem Cells.* Cell Stem Cell, 2010. **7**(3): p. 403-417, https://dx.doi.org/10.1016/j.stem.2010.07.010
3. Bellacosa, A., et al., *Altered Gene Expression in Morphologically Normal Epithelial Cells from Heterozygous Carriers of BRCA1 or BRCA2 Mutations.* Cancer Prevention Research, 2010. **3**(1): p. 48-61, https://doi.org/10.1158/1940-6207.CAPR-09-0078
4. Burga, L.N., et al., *Altered Proliferation and Differentiation Properties of Primary Mammary Epithelial Cells from BRCA1 Mutation Carriers.* Cancer Research, 2009. **69**(4): p. 1273-1278, https://doi.org/10.1158/0008-5472.CAN-08-2954
5. Shakya, R., et al., *The basal-like mammary carcinomas induced by Brca1 or Bard1 inactivation implicate the BRCA1/BARD1 heterodimer in tumor suppression.* Proceedings of the National Academy of Sciences, 2008. **105**(19): p. 7040-7045, https://www.pnas.org/doi/abs/10.1073/pnas.0711032105
6. Tao, L., et al., *Induced p53 loss in mouse luminal cells causes clonal expansion and development of mammary tumours.* Nature Communications, 2017. **8**(1): p. 14431, https://doi.org/10.1038/ncomms14431
7. Tao, L., Maaike P.A. van Bragt, and Z. Li, *A Long-Lived Luminal Subpopulation Enriched with Alveolar Progenitors Serves as Cellular Origin of Heterogeneous Mammary Tumors.* Stem Cell Reports, 2015. **5**(1): p. 60-74, https://www.sciencedirect.com/science/article/pii/S2213671115001575
8. Shehata, M., et al., *Phenotypic and functional characterisation of the luminal cell hierarchy of the mammary gland.* Breast Cancer Research, 2012. **14**(5): p. R134, https://dx.doi.org/10.1186/bcr3334
9. Bach, K., et al., *Time-resolved single-cell analysis of Brca1 associated mammary tumourigenesis reveals aberrant differentiation of luminal progenitors.* Nature Communications, 2021. **12**(1), https://dx.doi.org/10.1038/s41467-021-21783-3
10. Wysolmerski, J.J., et al., *Overexpression of parathyroid hormone-related protein or parathyroid hormone in transgenic mice impairs branching morphogenesis during mammary gland development.* Development, 1995. **121**(11): p. 3539-3547, https://doi.org/10.1242/dev.121.11.3539
11. Forster, N., et al., *Basal Cell Signaling by p63 Controls Luminal Progenitor Function and Lactation via NRG1.* Developmental Cell, 2014. **28**(2): p. 147-160, https://www.sciencedirect.com/science/article/pii/S1534580713007004
12. Olander, A. and S.S. Sikandar, *Branching out: the diverse roles of stem and progenitor cells in mammary gland development.* Journal of Mammary Gland Biology and Neoplasia, 2026. **31**(1): p. 13, https://doi.org/10.1007/s10911-026-09595-x
13. Gray, G.K., et al., *Defining breast epithelial cell types in the single-cell era.* Developmental Cell, 2025. **60**(17): p. 2218-2236, https://dx.doi.org/10.1016/j.devcel.2025.06.032
14. Runswick, S.K., et al., *Desmosomal adhesion regulates epithelial morphogenesis and cell positioning.* Nature Cell Biology, 2001. **3**(9): p. 823-830, https://doi.org/10.1038/ncb0901-823
15. Daniel, C.W., P. Strickland, and Y. Friedmann, *Expression and Functional Role of E- and P-Cadherins in Mouse Mammary Ductal Morphogenesis and Growth.* Developmental Biology, 1995. **169**(2): p. 511-519, https://www.sciencedirect.com/science/article/pii/S0012160685711657
16. Radice, G.L., et al., *Precocious mammary gland development in P-cadherin-deficient mice.* J Cell Biol, 1997. **139**(4): p. 1025-32,
17. Deugnier, M.-A., et al., *The importance of being a myoepithelial cell.* Breast Cancer Research, 2002. **4**(6): p. 224, https://doi.org/10.1186/bcr459
18. Sternlicht, M.D., et al., *The human myoepithelial cell is a natural tumor suppressor.* Clinical Cancer Research, 1997. **3**(11): p. 1949-1958,
19. Ingthorsson, S., et al., *Context-Dependent Function of Myoepithelial Cells in Breast Morphogenesis and Neoplasia.* Curr Mol Biol Rep, 2015. **1**(4): p. 168-174,
20. Sopel, M., *The myoepithelial cell: its role in normal mammary glands and breast cancer.* Folia Morphologica, 2010. **69**(1): p. 1,

https://proxy1.library.virginia.edu/login?url=https://www.proquest.com/scholarly-journals/myoepithelial-cell-role-normal-mammary-glands/docview/2464208698/se-2?accountid=14678
21. Pandey, P.R., *Role of myoepithelial cells in breast tumor progression.* Frontiers in Bioscience, 2010. **15**(1): p. 226, https://dx.doi.org/10.2741/3617
22. Sirka, O.K., E.R. Shamir, and A.J. Ewald, *Myoepithelial cells are a dynamic barrier to epithelial dissemination.* J Cell Biol, 2018. **217**(10): p. 3368-3381,
23. Man, Y.-g., et al., *The most likely but largely ignored triggering factor for breast (or all) cancer invasion.* Journal of Cancer, 2023. **14**(4): p. 573-590, https://www.jcancer.org/v14p0573.htm
24. Gudjonsson, T., et al., *Myoepithelial Cells: Their Origin and Function in Breast Morphogenesis and Neoplasia.* Journal of Mammary Gland Biology and Neoplasia, 2005. **10**(3): p. 261-272, https://dx.doi.org/10.1007/s10911-005-9586-4
25. Polyak, K. and M. Hu, *Do Myoepithelial Cells Hold the Key for Breast Tumor Progression?* Journal of Mammary Gland Biology and Neoplasia, 2005. **10**(3): p. 231-247, https://doi.org/10.1007/s10911-005-9584-6
26. Botti, G., et al., *Morphological and pathological features of basal-like breast cancer.* Transl Cancer Res, 2019. **8**(Suppl 5): p. S503-s509,
27. Thennavan, A., et al., *Molecular signatures of in situ to invasive progression for basal-like breast cancers: An integrated mouse model and human DCIS study.* npj Breast Cancer, 2022. **8**(1), https://dx.doi.org/10.1038/s41523-022-00450-w
28. Barsky, S.H. and N.J. Karlin, *Myoepithelial Cells: Autocrine and Paracrine Suppressors of Breast Cancer Progression.* Journal of Mammary Gland Biology and Neoplasia, 2005. **10**(3): p. 249-60, https://proxy1.library.virginia.edu/login?url=https://www.proquest.com/scholarly-journals/myoepithelial-cells-autocrine-paracrine/docview/219239487/se-2?accountid=14678
29. Wilson, G.M., et al., *Ductal Carcinoma in Situ: Molecular Changes Accompanying Disease Progression.* Journal of Mammary Gland Biology and Neoplasia, 2022. **27**(1): p. 101-131, https://dx.doi.org/10.1007/s10911-022-09517-7
30. Wang, J., et al., *Progression from ductal carcinoma in situ to invasive breast cancer: molecular features and clinical significance.* Signal Transduction and Targeted Therapy, 2024. **9**(1), https://dx.doi.org/10.1038/s41392-024-01779-3
31. Ding, L., et al., *Perturbed myoepithelial cell differentiation in BRCA mutation carriers and in ductal carcinoma in situ.* Nature Communications, 2019. **10**(1), https://dx.doi.org/10.1038/s41467-019-12125-5
32. Zeng, J., et al., *A genetic mosaic mouse model illuminates the pre-malignant progression of basal-like breast cancer.* Disease Models & Mechanisms, 2023. **16**(11), https://dx.doi.org/10.1242/dmm.050219
33. Ciwinska, M., et al., *Mechanisms that clear mutations drive field cancerization in mammary tissue.* Nature, 2024. **633**(8028): p. 198-206, https://dx.doi.org/10.1038/s41586-024-07882-3
34. Hannezo, E. and C.L.G.J. Scheele, *A Guide Toward Multi-scale and Quantitative Branching Analysis in the Mammary Gland*. 2023, Springer US. p. 183-205.
35. Davie, S.A., et al., *Effects of FVB/NJ and C57Bl/6J strain backgrounds on mammary tumor phenotype in inducible nitric oxide synthase deficient mice.* Transgenic Res, 2007. **16**(2): p. 193-201,
36. Zong, H., et al., *Mosaic Analysis with Double Markers in Mice.* Cell, 2005. **121**(3): p. 479-492, https://www.sciencedirect.com/science/article/pii/S0092867405001571
37. Lim, E., et al., *Aberrant luminal progenitors as the candidate target population for basal tumor development in BRCA1 mutation carriers.* Nature Medicine, 2009. **15**(8): p. 907-913, https://dx.doi.org/10.1038/nm.2000
38. Christin, J.R., et al., *Stem Cell Determinant SOX9 Promotes Lineage Plasticity and Progression in Basal-like Breast Cancer.* Cell Reports, 2020. **31**(10): p. 107742, https://www.sciencedirect.com/science/article/pii/S2211124720307221
39. Granit, R.Z., et al., *Regulation of Cellular Heterogeneity and Rates of Symmetric and Asymmetric Divisions in Triple-Negative Breast Cancer.* Cell Reports, 2018. **24**(12): p. 3237-3250, https://dx.doi.org/10.1016/j.celrep.2018.08.053
40. Proia, T.A., et al., *Genetic Predisposition Directs Breast Cancer Phenotype by Dictating Progenitor Cell Fate.* Cell Stem Cell, 2011. **8**(2): p. 149-163, https://dx.doi.org/10.1016/j.stem.2010.12.007

41. Sanawar, R. and S.K. Sengodan, *BRCA1: An Unrecognized Modulator of Lineage Plasticity in Basal-like Breast Cancer.* Journal of Mammary Gland Biology and Neoplasia, 2025. **31**(1): p. 1, https://doi.org/10.1007/s10911-025-09592-6
42. Bornes, L., et al., *The oestrous cycle stage affects mammary tumour sensitivity to chemotherapy.* Nature, 2025. **637**(8044): p. 195-204, https://dx.doi.org/10.1038/s41586-024-08276-1
43. Shao, Z.-M., et al., *The Human Myoepithelial Cell Exerts Antiproliferative Effects on Breast Carcinoma Cells Characterized by p21WAF1/CIP1Induction, G2/M Arrest, and Apoptosis.* Experimental Cell Research, 1998. **241**(2): p. 394-403, https://www.sciencedirect.com/science/article/pii/S0014482798940666
44. Emerman, J.T. and A.W. Vogl, *Cell size and shape changes in the myoepithelium of the mammary gland during differentiation.* The Anatomical Record, 1986. **216**(3): p. 405-415, https://dx.doi.org/10.1002/ar.1092160310
45. Glukhova, M., et al., *Adhesion systems in normal breast and in invasive breast carcinoma.* Am J Pathol, 1995. **146**(3): p. 706-16,
46. Gudjonsson, T., et al., *Normal and tumor-derived myoepithelial cells differ in their ability to interact with luminal breast epithelial cells for polarity and basement membrane deposition.* Journal of Cell Science, 2002. **115**(1): p. 39-50, https://dx.doi.org/10.1242/jcs.115.1.39
47. Hager, C., C. Jehanno, and M. Bentires-Alj, *Reactivation of Multipotency in the Mammary Gland – a Ripple in the Pond and a Turn of the Tide.* Journal of Mammary Gland Biology and Neoplasia, 2025. **30**(1): p. 11, https://doi.org/10.1007/s10911-025-09586-4
48. Muzumdar, M.D., L. Luo, and H. Zong, *Modeling sporadic loss of heterozygosity in mice by using mosaic analysis with double markers (MADM).* Proceedings of the National Academy of Sciences, 2007. **104**(11): p. 4495-4500, https://www.pnas.org/doi/abs/10.1073/pnas.0606491104
49. Martins, F.C., et al., *Evolutionary Pathways in BRCA1-Associated Breast Tumors.* Cancer Discovery, 2012. **2**(6): p. 503-511, https://doi.org/10.1158/2159-8290.CD-11-0325
50. Nee, K., et al., *Preneoplastic stromal cells promote BRCA1-mediated breast tumorigenesis.* Nature Genetics, 2023. **55**(4): p. 595-606, https://dx.doi.org/10.1038/s41588-023-01298-x
51. Zeng, J., *Premalignant Development of BRCA-1-associated Ovarian & Breast Cancer*. 2023, University of Virginia, Microbiology - School of Medicine, PHD (Doctor of Philosophy), 2023: Charlottesville, VA.
52. Chi, J., et al., *Three-Dimensional Adipose Tissue Imaging Reveals Regional Variation in Beige Fat Biogenesis and PRDM16-Dependent Sympathetic Neurite Density.* Cell Metabolism, 2018. **27**(1): p. 226-236.e3, https://dx.doi.org/10.1016/j.cmet.2017.12.011
53. Lloyd-Lewis, B., et al., *Imaging the mammary gland and mammary tumours in 3D: optical tissue clearing and immunofluorescence methods.* Breast Cancer Research, 2016. **18**(1), https://dx.doi.org/10.1186/s13058-016-0754-9
54. Van Keymeulen, A., et al., *Reactivation of multipotency by oncogenic PIK3CA induces breast tumour heterogeneity.* Nature, 2015. **525**(7567): p. 119-123, https://dx.doi.org/10.1038/nature14665
55. Koren, S., et al., *PIK3CAH1047R induces multipotency and multi-lineage mammary tumours.* Nature, 2015. **525**(7567): p. 114-118, https://dx.doi.org/10.1038/nature14669
56. Hein, S.M., et al., *Luminal epithelial cells within the mammary gland can produce basal cells upon oncogenic stress.* Oncogene, 2016. **35**(11): p. 1461-1467, https://dx.doi.org/10.1038/onc.2015.206
57. Bai, F., et al., *Germline mutation of Brca1 alters the fate of mammary luminal cells and causes luminal-to-basal mammary tumor transformation.* Oncogene, 2013. **32**(22): p. 2715-2725, https://doi.org/10.1038/onc.2012.293
58. Rios, A.C., et al., *The complexities and caveats of lineage tracing in the mammary gland.* Breast Cancer Research, 2016. **18**(1): p. 116, https://doi.org/10.1186/s13058-016-0774-5
59. Hannezo, E. and C.L.G.J. Scheele, *A Guide Toward Multi-scale and Quantitative Branching Analysis in the Mammary Gland*, in *Cell Migration in Three Dimensions*, C. Margadant, Editor. 2023, Springer US: New York, NY. p. 183-205.

Figures

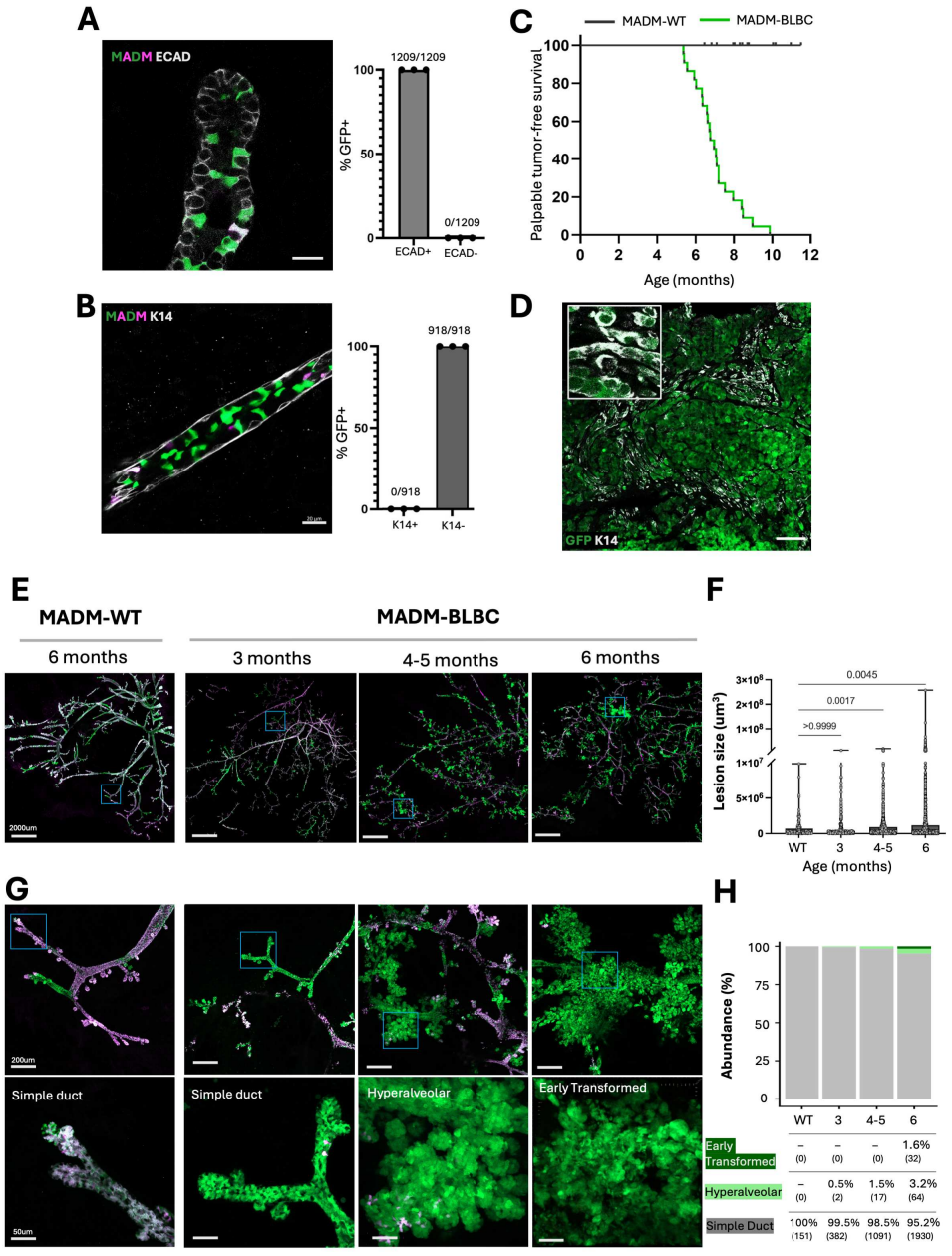


Figure 0

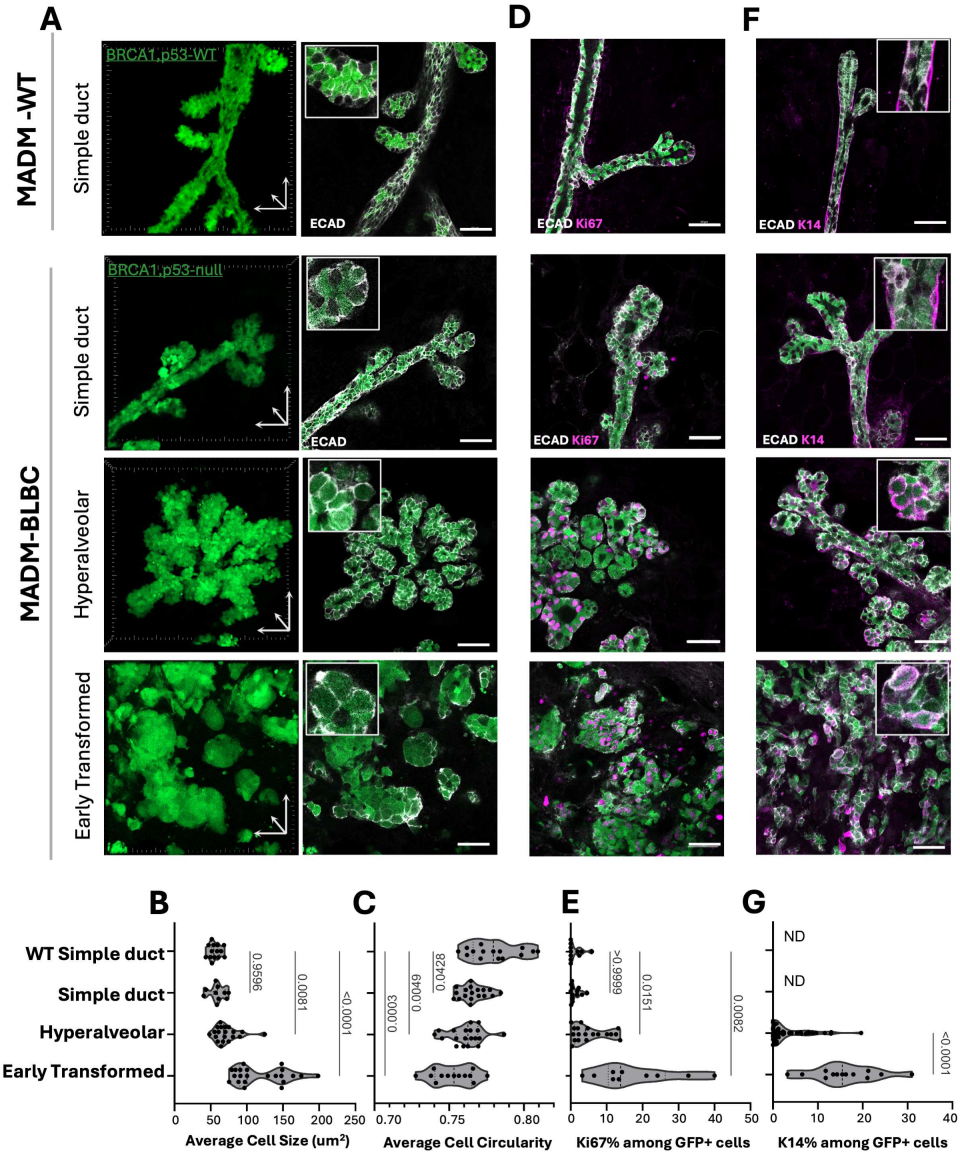

A
D
F
MADM -WT
Simple duct
BRCA1;p53-WT
ECAD
ECAD Ki67
ECAD K14
MADM-BLBC
Simple duct
BRCA1;p53-null
Hyperalveolar
Early Transformed
B
C
E
G
WT Simple duct
Simple duct
Hyperalveolar
Early Transformed
0.9696
0.0081
<0.0001
0.0003
0.0049
0.0428
>0.9999
0.0151
0.0082
ND
ND
<0.0001
Average Cell Size (um²)
Average Cell Circularity
Ki67% among GFP+ cells
K14% among GFP+ cells

Figure 1

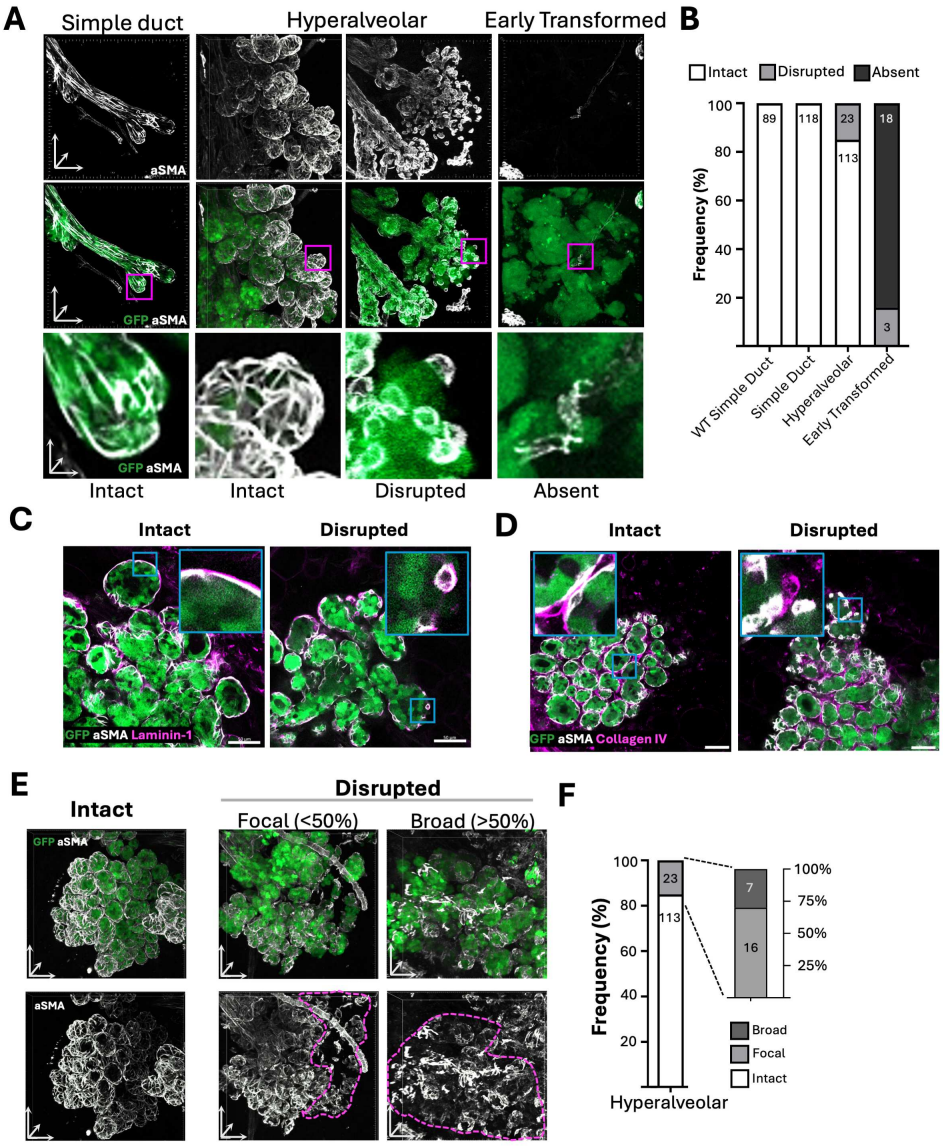

A
Simple duct
Hyperalveolar
Early Transformed
aSMA
GFP aSMA
GFP aSMA
Intact
Intact
Disrupted
Absent
B
Intact
Disrupted
Absent
Frequency (%)
100
80
60
40
20
89
118
23
113
18
3
WT Simple Duct
Simple Duct
Hyperalveolar
Early Transformed
C
Intact
Disrupted
GFP aSMA Laminin-1
D
Intact
Disrupted
GFP aSMA Collagen IV
E
Intact
Disrupted
Focal (<50%)
Broad (>50%)
GFP aSMA
aSMA
F
Frequency (%)
100
80
60
40
20
23
113
7
16
100%
75%
50%
25%
Broad
Focal
Intact
Hyperalveolar

Figure 2

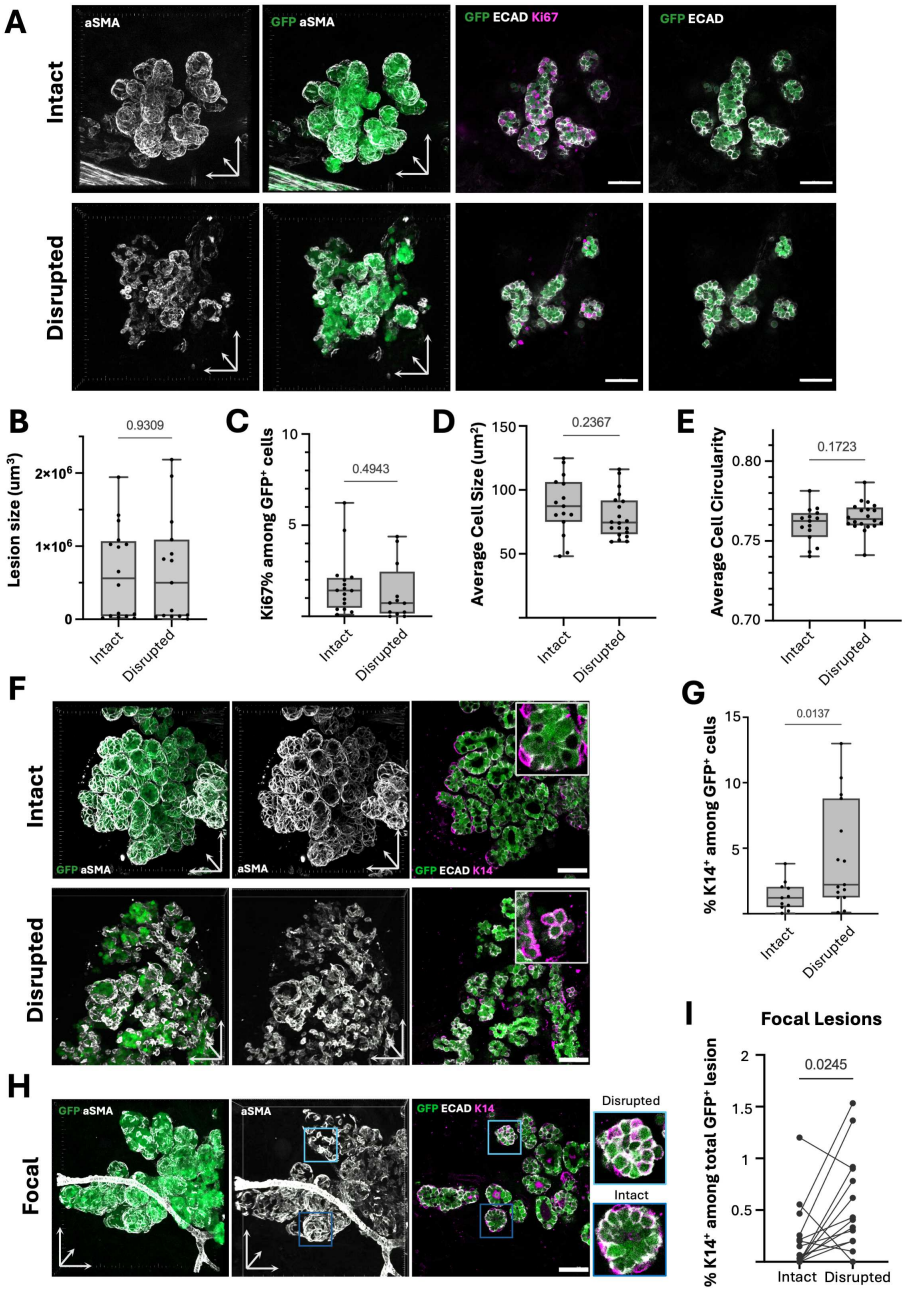

A
aSMA
GFP aSMA
GFP ECAD Ki67
GFP ECAD
Intact
Disrupted
B
Lesion size (um³)
0.9309
C
Ki67% among GFP⁺ cells
0.4943
D
Average Cell Size (um²)
0.2367
E
Average Cell Circularity
0.1723
Intact
Disrupted
F
GFP aSMA
aSMA
GFP ECAD K14
G
% K14⁺ among GFP⁺ cells
0.0137
H
Focal
I
Focal Lesions
% K14⁺ among total GFP⁺ lesion
0.0245

Figure 3

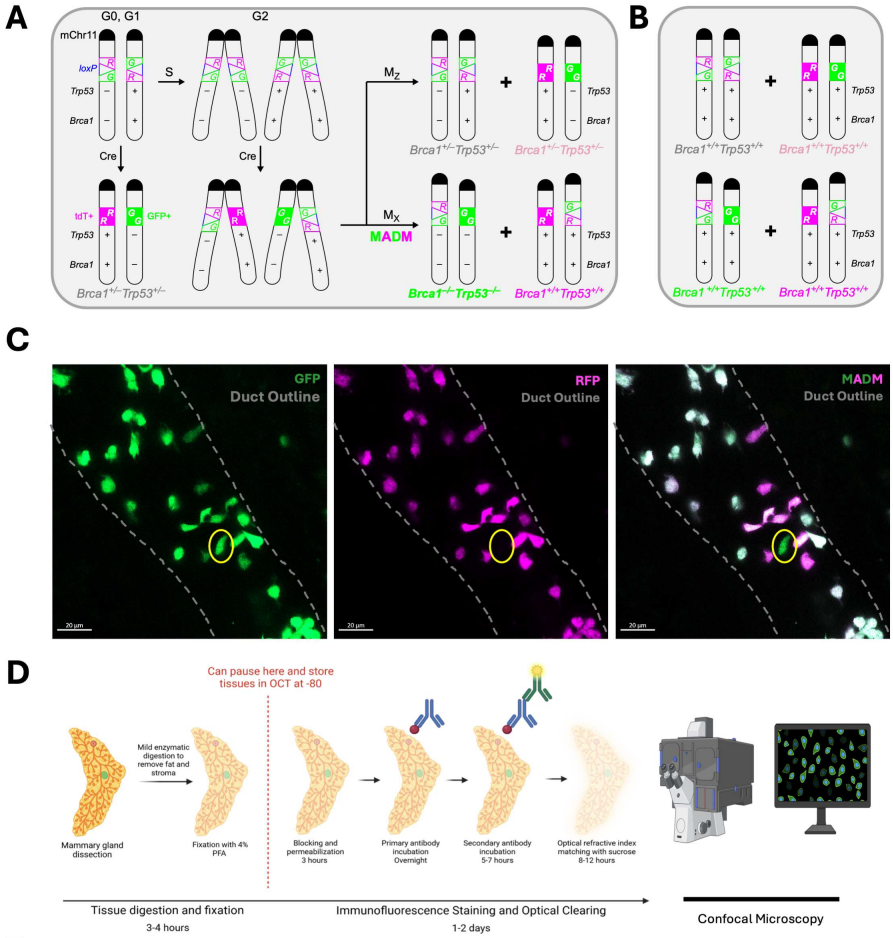

A
G0, G1
G2
mChr11
loxP
Trp53
Brca1
S
Cre
Cre
tdT+
GFP+
Brca1+/–Trp53+/–
Mz
Mx
MADM
Brca1+/–Trp53+/–
Brca1+/–Trp53+/–
Brca1–/–Trp53–/–
Brca1+/+Trp53+/+
B
Brca1+/+Trp53+/+
Brca1+/+Trp53+/+
Brca1+/+Trp53+/+
Brca1+/+Trp53+/+
C
GFP
Duct Outline
RFP
Duct Outline
MADM
Duct Outline
20 µm
D
Can pause here and store tissues in OCT at -80
Mild enzymatic digestion to remove fat and stroma
Mammary gland dissection
Fixation with 4% PFA
Blocking and permeabilization 3 hours
Primary antibody incubation Overnight
Secondary antibody incubation 5-7 hours
Optical refractive index matching with sucrose 8-12 hours
Tissue digestion and fixation
3-4 hours
Immunofluorescence Staining and Optical Clearing
1-2 days
Confocal Microscopy
E
MADM
Imaris GFP mask
1000 µm

Figure 4

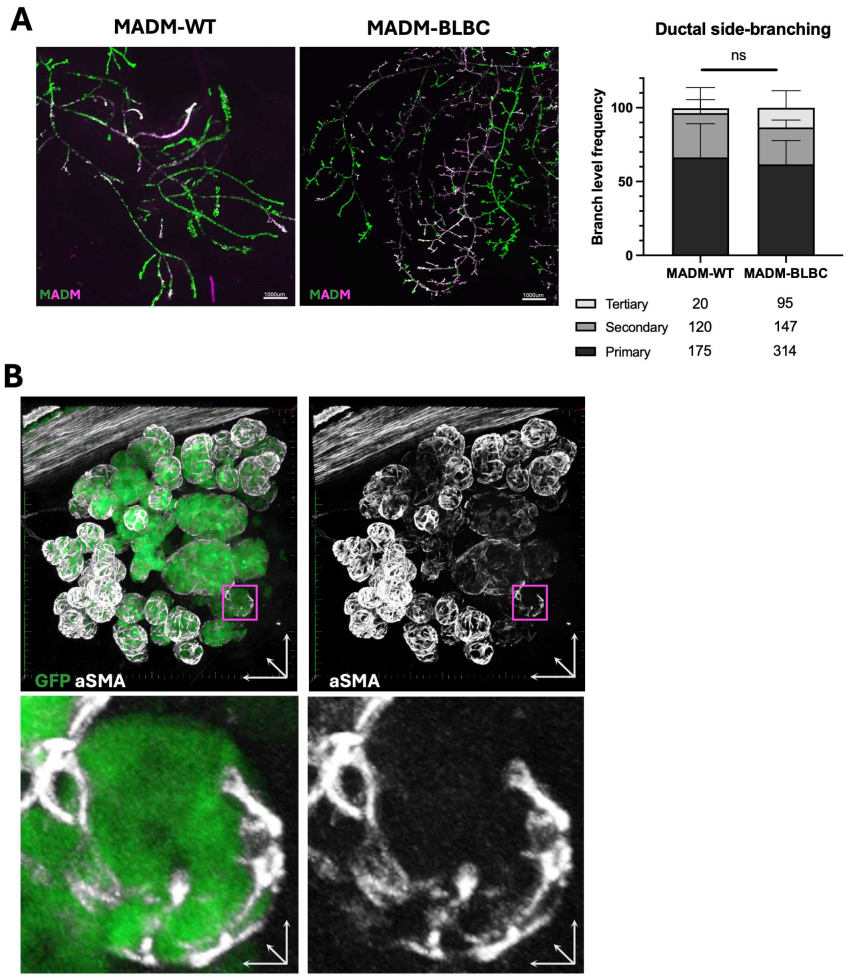

A
MADM-WT
MADM-BLBC
MADM
MADM
Ductal side-branching
ns
Branch level frequency
100
50
0
MADM-WT
MADM-BLBC
Tertiary 20 95
Secondary 120 147
Primary 175 314
B
GFP aSMA
aSMA

Figure 5